ROYAL SOCIETY
OF CHEMISTRY

EDGE ARTICLE

Check for updates

CoeffNet: predicting activation barriers through a chemically-interpretable, equivariant and physically constrained graph neural network†

Sudarshan Vijay, [iD] ab Maxwell C. Venetos, ab Evan Walter Clark Spotte-Smith, [iD] ab Aaron D. Kaplan, b Mingjian Wen c and Kristin A. Persson*ad

Activation barriers of elementary reactions are essential to predict molecular reaction mechanisms and kinetics. However, computing these energy barriers by identifying transition states with electronic structure methods (*e.g.*, density functional theory) can be time-consuming and computationally expensive. In this work, we introduce *CoeffNet*, an equivariant graph neural network that predicts activation barriers using coefficients of any frontier molecular orbital (such as the highest occupied molecular orbital) of reactant and product complexes as graph node features. We show that using coefficients as features offer several advantages, such as chemical interpretability and physical constraints on the network's behaviour and numerical range. Model outputs are either activation barriers or coefficients of the chosen molecular orbital of the transition state; the latter quantity allows us to interpret the results of the neural network through chemical intuition. We test *CoeffNet* on a dataset of S_N2 reactions as a proof-of-concept and show that the activation barriers are predicted with a mean absolute error of less than 0.025 eV. The highest occupied molecular orbital of the transition state is visualized and the distribution of the orbital densities of the transition states is described for a few prototype S_N2 reactions.

I. Introduction

Activation barriers computed using *ab initio* methods have greatly facilitated mechanistic understanding of reactions occurring in battery electrolytes,[1–4] catalysis,[5–8] organic synthesis[9] and many other fields of chemistry.[10,11] The activation barrier is determined as the energy difference between a first-order saddle point (a transition state) and a local minimum of the potential energy surface (a reactant or product), which provides insight into the likelihood of a reactant converting into a product. A large activation barrier implies that the reaction is sluggish, while fast chemical reactions have small activation barriers.

Activation barriers are often computed using electronic structure methods like density functional theory (DFT). In

practice, these computations are usually not straightforward to perform. They can be time-consuming, requiring multiple gradient evaluations for an optimizer to identify a first-order saddle point. They are also difficult to automate, as transition state optimizations are very sensitive to the choice of the initial guessed structure. Even when an optimization successfully converges, it frequently produces an unwanted transition state.[12]

Several models have been proposed to approximate the activation barrier to circumvent the need for explicitly performing transition-state finding calculations. A fundamental assumption of these models is that the activation barrier can be expressed as a function of a handful of variables determined from the electronic structure of the reactants and products alone. The simplest such model is the Brønsted–Evans–Polanyi (BEP) relation,[13–16] which assumes a linear relationship between the activation barrier and energy difference between reactants and products. More complex models consider other potential energy surface (PES) complexities, such as solvent reorganization in Marcus theory.[17–21] While these models work well for a narrow chemical space and are chemically interpretable, they need to be re-parameterized for even the slightest change to the chemistry and conditions, such as for example, different ligands around a fixed reaction centre.

Machine learning models offer an alternative to determining activation barriers without relying on assumptions about the

aDepartment of Materials Science and Engineering, University of California, Berkeley, 210 Hearst Memorial Mining Building, Berkeley, CA, 94720 USA. E-mail: kristinpersson@berkeley.edu

bMaterials Science Division, Lawrence Berkeley National Laboratory, 1 Cyclotron Road, Berkeley, CA, 94720 USA

cDepartment of Chemical and Biomolecular Engineering, University of Houston, Houston, Texas 77204, USA

dThe Molecular Foundry, Lawrence Berkeley National Laboratory, 1 Cyclotron Road, Berkeley, CA, 94720 USA

PES, such as in BEP and Marcus-theory-based models.[22] Current machine-learning models used to determine activation barriers range from methods using active-learning routines,[23] to one-shot kernel-methods[24] or neural network[25–27] predictions. Active learning routines require iteratively performed DFT calculations, and one-shot predictions require a significant number (between 2000 and 12 000) of DFT calculations as a part of their training data sets. In general, these approaches lack chemical interpretability in their outputs.

In this work, we introduce *CoeffNet*, a graph-neural network (GNN) that is capable of predicting both the activation energies and the frontier orbitals, such as the highest-occupied molecular orbital (HOMO) of the transition state. Inputs to the model are the coefficients of any frontier molecular orbitals of reactant and product complexes which are outputs of any localized-basis electronic structure code. Our approach of using coefficients of molecular orbitals offers three advantages: (1) inductive bias in the form of an idealized description of the variation of the electronic structure from reactant to transition state, which is a common feature of theoretical models enabling accurate activation barrier predictions (2) physical constraints imposed on the features used to parameterize the GNN allowing the model to learn within a fixed numerical range, and (3) chemical interpretability of the predicted output, which is any molecular orbital of the transition state. A key use-case of *CoeffNet* is to accurately predict activation barriers and offer chemical interpretability when applied to a fixed class of reactions. When applied to a diverse database of reactions, it acts as a pre-sieving tool to provide a coarse estimate of the activation barrier such that only those reactions with chemically interesting activation barriers may be computed using computationally intensive transition state search DFT calculations. This manuscript is organized as follows: in Section II, we discuss the features of the coefficients of frontier orbitals and how they incorporate inductive bias when used as features in *CoeffNet*. In Section III, we describe the architecture of *CoeffNet*. As a proof-of-concept, we apply it to predict activation barriers and the HOMO for selected S_N2 reactions. Finally, in Section IV, we show that the model outputs align with chemical intuition.

II. Coefficients of frontier orbitals serve as a gauge of reactivity

In this section, we motivate our choice of coefficients of a molecular orbital as features for *CoeffNet*. We briefly describe how these coefficients are defined in the context of DFT and how they change for different molecular orbitals as a function of the rotation of a molecule and along a reaction path from reactant to transition state to product. We note that the example of analysing the orbitals of water is a simple one, where we illustrate the interpretive role that coefficients provide. We defer more chemically relevant examples to Section S3† and Section IV of this manuscript.

Localized-basis DFT codes compute a chosen molecular orbital, ψ_i, through a linear combination of all multiple atom-centred atomic orbitals, ϕ_j consisting of s, p, d, and higher basis functions. C_{ij} contains the relative weights of atomic orbital j in a molecular orbital with index i,

$$\psi_i(\mathbf{r}) = \sum_j^{N_{\text{basis}}} C_{ij}\phi_j(\mathbf{r}), \tag{1}$$

where N_{basis} are the total number of atomic orbitals used in a DFT calculation, and $\mathbf{r}$ are positions in Cartesian space. C_{ij} is determined iteratively by a self-consistent field (SCF) procedure through the generalized eigenvalue problem, $\mathbf{FC} = \varepsilon\mathbf{SC}$ where $\mathbf{F}$ is the matrix representation of the Kohn–Sham Hamiltonian, $\mathbf{C}$ is the matrix of coefficients for all molecular orbitals, ε are the eigenvalues of the molecular orbitals and $\mathbf{S}$ is the overlap matrix (*i.e.* the overlap between any two atomic orbitals j and j' in matrix form).[28] From $\mathbf{C}$, one can immediately determine reduced density matrices, the local density, and their gradients.

For a given ψ_i, we think of C_{ij} as informing us as to what ϕ_j, and hence what atoms are reactive. Consider C_{ij} for selected molecular orbitals of water shown in Fig. 1a. For the HOMO (column corresponding to an x-axis value of -7.93 eV, *i.e.* the least negative x-axis value), we find that the largest value of $|C_{ij}|$ (in red) appears for oxygen p-orbitals and hydrogen p-orbitals (polarization functions). This result matches our expectations on the reactivity of water; the oxygen lone-pairs (composed of p-orbitals), as well as additional hydrogen-bond-forming orbitals of hydrogen, are likely to be the most reactive. All ψ's that are lower in energy, such as those corresponding to an eigenvalue of -9.96 eV, include deeply buried ϕ_j, such as the s-functions of oxygen and hydrogen, which are less reactive. Unoccupied molecular orbitals (where the x-axis is positive) are largely made up of polarization functions. Passing this information to *CoeffNet* will inform it of orbital-level, environment-specific reactivity. In Section S3† we discuss the case where multiple molecular orbitals might be needed to correctly represent reactivity through the example of coefficients of the molecular orbital of pyridine, where a combination of HOMO and the eigenstate below the HOMO are needed to properly represent the reactive centers of the molecule.[29]

A. Numerical properties of C

A useful property of C_{ij} is that it can take values strictly between -1 to 1 when determined in orthonormal basis and for real-valued functions (see Section S1† for converting from non-orthonormal to orthonormal basis). Furthermore,

$$\sum_j^{N_{\text{basis}}} |C_{ij}|^2 = 1, \tag{2}$$

i.e. the sum of squares of C_{ij} for a single molecular orbital in orthonormal basis is 1. In a practical context, these constraints mean that the relative weights of ϕ that make ψ are normalized, and any prediction of C_{ij} will only need to operate within a narrow range of numerical values.

While $\mathbf{C}$ provides intuitive molecular-orbital level information, as well as constraints on attainable numerical values, it is sensitive to both rotation and sign change. Fig. 1b shows $\mathbf{C}$ for
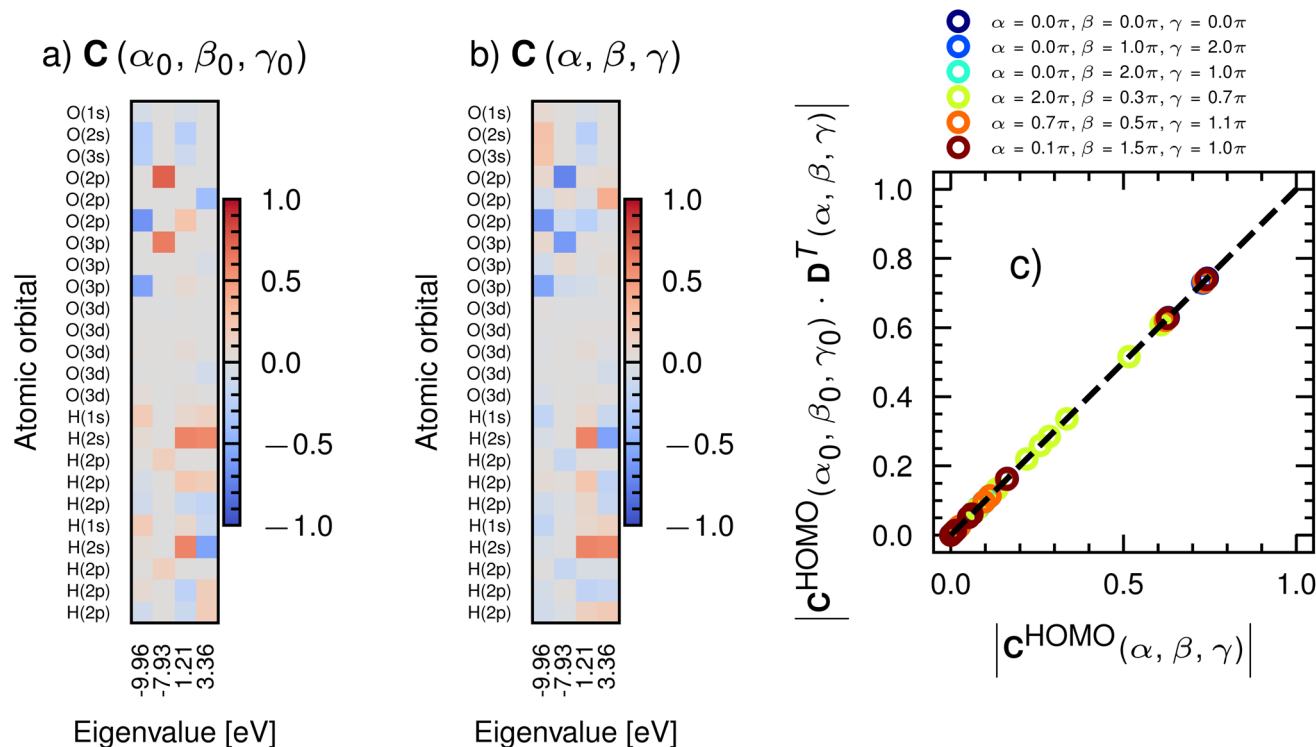
Fig. 1 (a) Coefficient matrix for selected eigenvalues (x-axis) and all atomic orbital basis functions (y-axis) used in a DFT calculation of H_2O at a certain Euler angle $(\alpha_0, \beta_0, \gamma_0)$ about the origin of a cartesian coordinate system with the def2-SVP basis set; colors indicate the weight of a particular atomic orbital in that molecular orbital. (b) Same representation as (a), except at a different Euler angle (α, β, γ); note that both the sign and magnitude for each type of basis function (s, p, d) differ from (a). (c) The coefficient matrix rotates reliably from $\alpha_0 \to \alpha$, $\beta_0 \to \beta$ and $\gamma_0 \to \gamma$ through the D-matrix of rotation; legend shows Euler angles (α, β, γ) in radians.

water at a different orientation than shown in Fig. 1a (denoted by an Euler angle change $\alpha_0 \to \alpha$, $\beta_0 \to \beta$ and $\gamma_0 \to \gamma$ with a rotation matrix defined through an extrinsic rotation about the origin of cartesian coordinates). Note that both absolute values and signs are altered by this rotation. $\mathbf{C}$ is an eigenvector and hence accurate only up to a sign change (multiplying the eigenvalue problem ± 1 has no effect on the solution) and rotation changes the relative weights of p_x, p_y, p_z, d_{xy}, d_{yz}, d_{zx}, $d_{3z^2-r^2}$ and $d_{x^2-y^2}$ contributions to ψ. However, it is known that $\mathbf{C}$ rotates predictably, i.e.

$$\mathbf{C}(\alpha, \beta, \gamma) = \mathbf{C}(\alpha_0, \beta_0, \gamma_0) \cdot \mathbf{D}^T(\alpha, \beta, \gamma), \quad (3)$$

where $\mathbf{D}$ is the Wigner-D matrix.[30] Fig. 1c shows that there is a clear agreement between DFT computed absolute values of $\mathbf{C}(\alpha, \beta, \gamma)$ and those obtained from eqn (3) starting from $(\alpha_0, \beta_0, \gamma_0)$ (see Section S2† for a discussion on practical implementation). We utilize this property of reliable rotation while constructing the equivariant components of *CoeffNet*. In the rest of this manuscript, we drop the subscripts on C_{ij} for clarity, instead referring to $\mathbf{C}$ as the coefficients of a *single* molecular orbital for a given spin channel.

B. Variation of C from reactant to transition state to product

A final useful property of $\mathbf{C}$ is that it changes expectedly with chemical intuition along a reaction path. Fig. 2a shows selected

basis functions of atomic orbitals (y-axis) for the HOMO of reactant, transition state and product species for a prototype S_N2 reaction taken from ref. 31. The reaction follows the template

$$A + X^- \to B + Y^- \quad (4)$$

where A and B are species with a carbon backbone (R_3C-CR_3, where R is any substituent) and X^- and Y^- are attacking and leaving groups respectively.

In this particular S_N2 reaction, the chlorine atom (X^-) moves towards the carbon atom, while the fluorine atom (Y^-) leaves with a charge of -1. Nitrogen and hydrogen atoms are close to the reaction centre. Matching chemical intuition, the p-orbitals of chlorine have a higher weight in the product state (i.e. these orbitals contribute significantly to the HOMO and hence are involved in the bonding state of the species), while the p-orbitals of fluorine have a higher weight in the reactant state; the transition state has an intermediate weight between chlorine and fluorine p-orbitals. As expected through chemical intuition, bystander atoms nitrogen (p-orbitals) and hydrogen (s-orbital) have intermediate weight throughout the reaction.

C. Constructing a smaller representation of C

Most modern basis sets contain several polarization and diffuse functions (extra basis functions with higher angular quantum
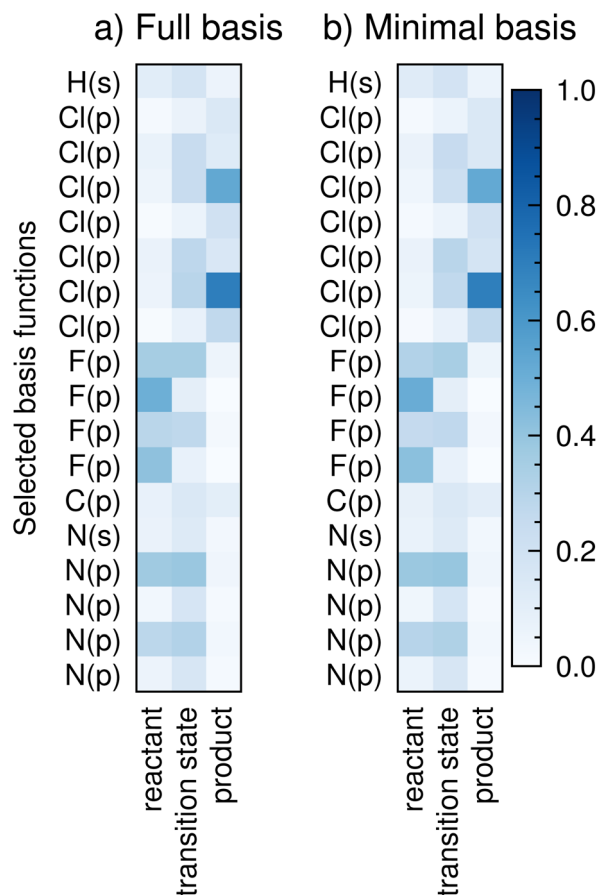
a) Full basis   b) Minimal basis

Fig. 2 Variation of the absolute value of the coefficients of the HOMO (visualized only for selected basis functions, *i.e.* the *y*-axis) from reactant → transition state → product for (a) full-basis representation, (*i.e.* as computed) and (b) minimal basis representation (see text).

numbers, l, such as d, f, g and h functions for small organic molecules, where only s and p functions are needed to fill all electrons). These extra basis functions are likely to render an intuitive understanding of **C** less straightforward. While they may provide more information to *CoeffNet*, they will also lead to a model that is more expensive to train. To explore the effect of reduction in the number of atomic orbitals *a posteriori* of a DFT calculation, we construct a smaller, *minimal* basis set from the *full* basis by the direct-projection method.[32] As an illustration of this idea, we select all s and p functions to constitute a minimal basis representation, ϕ_j^{m}, which constitutes of a subset of basis functions present in ϕ_j. This choice of minimal-basis set is consistent with the classes of molecules tested in this work (small organics with halogens) and can be tuned to include or exclude any atomic orbitals. If the number of basis functions in the minimal set is $M_{\mathrm{basis}}(<N_{\mathrm{basis}})$, then we define a rectangular matrix projection, $\mathbf{P} = \langle \phi_j^{\mathrm{m}} | \psi_i \rangle$ with dimensions $M_{\mathrm{basis}} \times N_{\mathrm{basis}}$. This projection is used to determine a minimal-basis Hamiltonian matrix, $\mathbf{F}^m = \mathbf{P}\boldsymbol{\varepsilon}\mathbf{P}^{\mathrm{T}}$ which is diagonalized to get the coefficients and eigenvalues in the minimal-basis representation. Fig. 2b shows **C** in a minimal-basis representation for the same S_N2 reaction shown in Fig. 2a. Both Fig. 2a and b convey

the same information for the relevant atoms, with only minor changes in numerical values for the minimal basis representation compared to the full basis representation. Thus, choosing a smaller basis set leads to a minimal loss of information (apart from the atomic orbitals that have purposefully been removed) for the examples we consider in this manuscript, allowing us to work with a smaller representation.

In summary, molecular orbitals represented through **C** present a chemically intuitive representation of reactivity, which we use as features in a graph neural network to learn quantities such as the activation barrier. **C** can also be converted to a smaller, minimal-basis representation without much information loss, allowing for a simpler learning process. In the next section, we discuss how *CoeffNet* uses **C** as a feature to learn activation barriers and molecular orbitals.

III. Equivariant graph-neural network to predict activation barriers

In this section, we describe the architecture of *CoeffNet*, and, as a proof-of-concept, we test its performance on the S_N2 reaction dataset.[31] We discuss how inputs are pre-processed to be amenable to use with commonly available graphs neural network architectures. We illustrate how learnt weights of the model allow it to predict both the activation barrier and **C** for a particular molecular orbital of the transition state.

Fig. 3a shows a schematic of the required inputs to *CoeffNet*, which are the geometry optimized positions ($\mathbf{r}$), atomic numbers ($\mathbf{v}$), **C** for reactant and product complexes and the free energy difference, ΔG, of the reaction going from reactant to product. Note that all inputs are readily obtained from DFT calculations on reactant and product complexes.

A. Pre-processing of inputs to node and edge attributes and features

We begin by generating graphs for both reactant and product complexes. The nodes of each graph represent atoms in a complex, and the edges represent the connectivity between these atoms. We choose to express this connectivity through a fixed cutoff, *i.e.* an atom in a complex is connected to all other atoms in its neighbourhood up to a fixed cutoff distance (which is left as a hyperparameter). We determine the distance between any two nodes, A and B, as the norm of the vector of their relative positions, $|\mathbf{r}_{\mathrm{A}} - \mathbf{r}_{\mathrm{B}}|$ (see schematic in Fig. 3a).

After creating the graphs for the reactant and product, we parameterize it with attributes using inputs illustrated in Fig. 3a. These attributes are fundamental properties of the node and edges they describe and are *not* altered by learnt weights. Each node is represented by a one-hot encoding of its atomic number. Each edge is parameterized by a normalized soft one-hot encoding[33] of the edge length. In practice, the edge length is expanded on a grid based on a fixed number of Gaussian basis functions.

We use **C** to generate node features which are to be modified by learnt weights. Since each atom has a different number of atomic orbitals, we need to pre-process **C** before it can be used
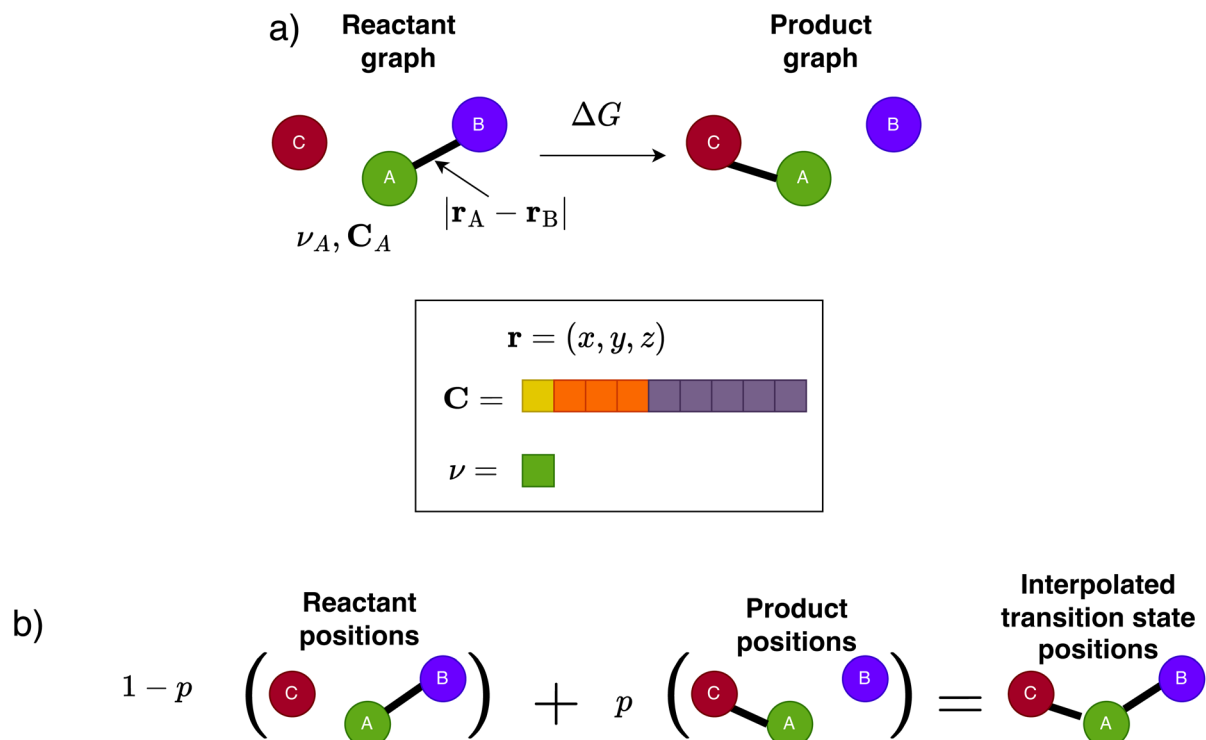
Fig. 3 (a) Inputs to *CoeffNet* are reactant and product atom positions, **r**, atomic numbers for each atom *ν*, and coefficients of a chosen eigenvalue **C**. (b) Schematic of the linear interpolation ($p \in [0, 1]$) used to determine the interpolated transition state graph.

as node features. This pre-processing is required as we use a graph with the same dimension of node features for all nodes and edge features for all edges. We split **C** into different atom-wise chunks based on which atom the atomic-orbital is centred on. These chunks are then normalized to be of the same dimension for all atoms by padding smaller chunks with zeros in an orbital-wise fashion. For example, in the case of a minimal basis representation of H_2O, the oxygen node will have the largest number of orbitals (two s functions with $l = 0$ and three p functions, with $l = 1$ for a total dimension of five). The

hydrogen node features would have exactly one s orbital; the other four dimensions (remaining one s and three p functions) are padded with zeros to make a total dimension of five.

B. Interpolation scheme to generate approximate transition state graphs and features

Having generated reactant and product graphs and parameterized them with node features, we now discuss how we generate transition state graphs and their associated node
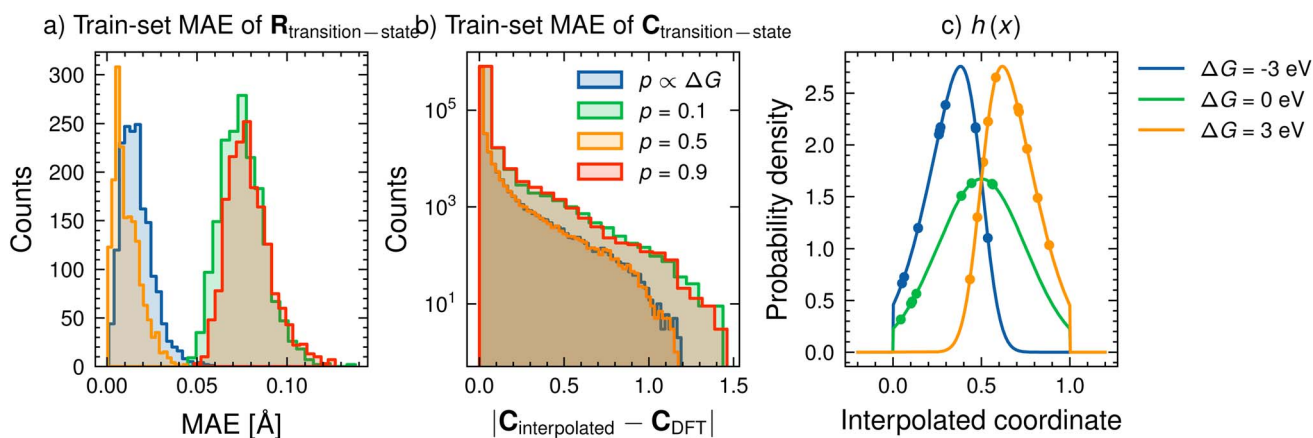

Fig. 4 (a) The mean-absolute error of the interpolated structure as compared with the real transition state structure for S_N2 reactions. (b) Absolute error between the interpolated and DFT **C** for the HOMO of the transition state (c) (lines) truncated skew-normal distribution $h(x)$ for three different $\Delta G = -3, 0, 3$ eV; $\mu = 0.5$, $\sigma = 0.25$, $\alpha = \Delta G$; (points) ten randomly sampled points from h for each ΔG.
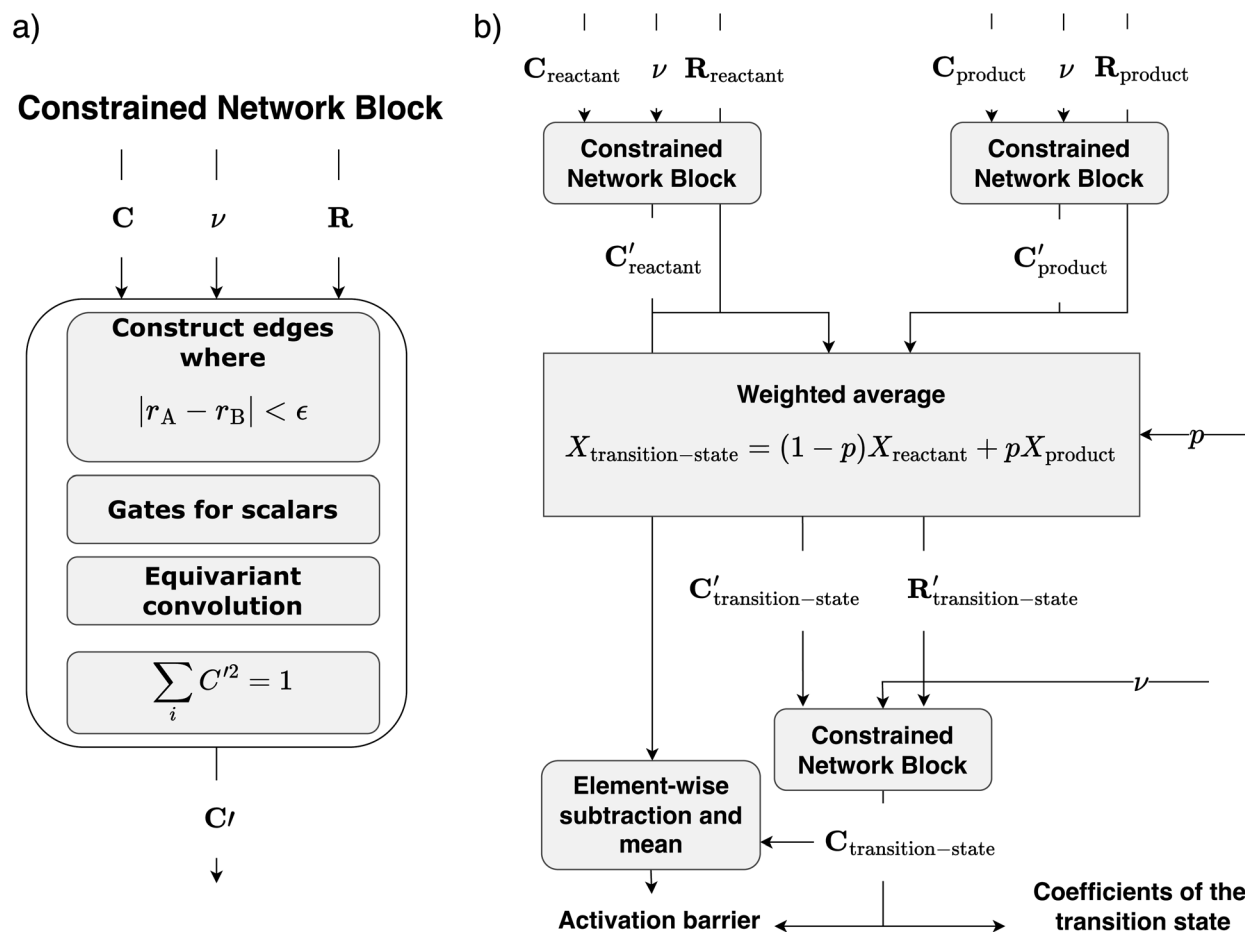
Fig. 5 (a) Schematic of a constrained network block with inputs of C, ν and R (see text for description). (b) Schematic of the architecture of *CoeffNet*; C, ν and R for both reactants and products are passed through a constrained network block shown in (a). C′, which is the output of the network, and R are linearly interpolated through p and are used as node features of the interpolated transition state graph. Outputs of the last network are interpreted either as coefficients of the molecular orbital or are averaged after subtraction with the outputs of the constrained network block of the reactants to get the activation barrier.

features. Generating this information is a necessary intermediate step to *CoeffNet*. Note that we cannot use the same method of graph generation as described in the previous section for reactant and product states, as we do not have access to the structure of the transition state as an input.

We use linear interpolation to generate an approximate representation of the transition state quantities from reactant and product quantities (see Fig. 3b for a schematic of this interpolation). For any quantity $\mathbf{X}$,

$$\mathbf{X}_{\text{transition-state}} = (1 - p)\mathbf{X}_{\text{reactant}} + p\mathbf{X}_{\text{product}}. \quad (5)$$

where subscripts to $\mathbf{X}$ indicate the quantity at that state (for example, $\mathbf{X}_{\text{transition-state}}$ represents $\mathbf{X}$ at the transition state) and p is a single scalar used as a sliding scale between reactant structure ($p = 0$) and product structure ($p = 1$). In this work, we linearly interpolate two quantities (1) $\mathbf{R}$, which is the $N \times 3$ (where N is the number of atoms) matrix of atom positions in a given structure and (2) $\mathbf{C}$, represented through the node features in the same dimensions as the reactant and product

graphs. In general, any scalar $p \in [0, 1]$ can be used to perform this interpolation.

We note that our objective through this interpolation scheme is not to predict accurate transition state structures or $\mathbf{C}$ (the latter is an output of *CoeffNet*) but to incorporate as much useful information as possible into an approximate transition state graph.

We start by assessing the feasibility of using a constant value of p. To test this method, we compare the mean absolute error (MAE) between $\mathbf{R}_{\text{transition-state}}$ obtained through eqn (5) and from DFT. Fig. 4a shows the MEA for different values of p for the training dataset for $p = 0.1$ (green), $p = 0.5$ (yellow) and $p = 0.9$ (red). We report the performance on the training dataset as the choice of p is made before training and kept fixed throughout training and inference. For our chosen proof-of-concept dataset, all values of p perform suitably well, with only minor differences in MAE of positions (less than 0.15 Å). Fig. 4b compares the absolute error between the interpolated and DFT computed $\mathbf{C}$ for the same values of p as in Fig. 4a. Several elements already have negligibly small errors prior to any
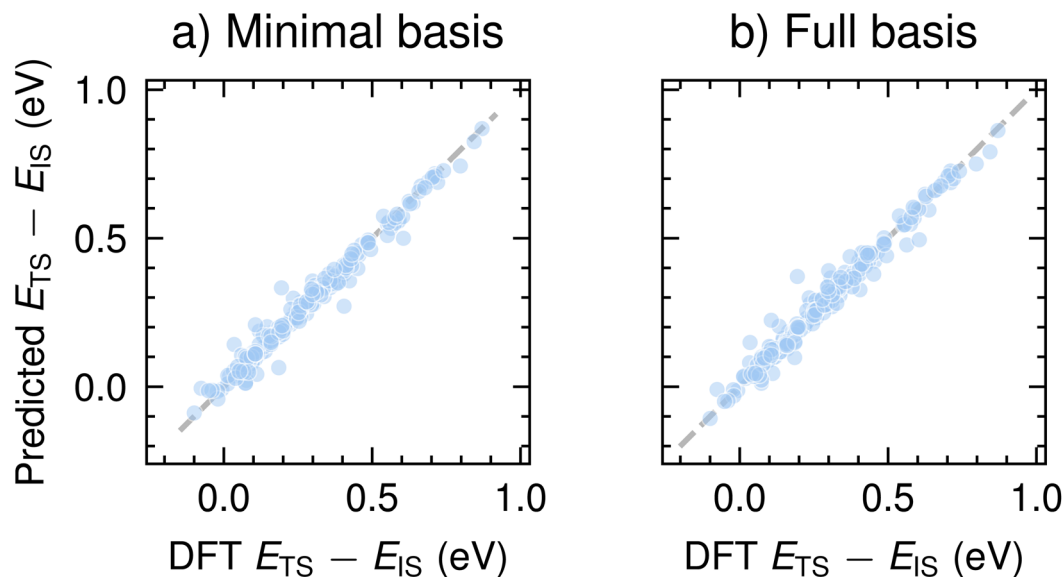
a) Minimal basis

b) Full basis

Fig. 6 Comparison of predicted activation barriers and DFT computed barriers on the test set for (a) minimal–basis representation (*i.e.* only s and p basis functions), and (b) full–basis (*i.e.* as computed with DFT) for the def2-SVP basis set. See Fig. S7† for a corresponding plot for barriers computed with the def2-TZVP basis set.

Table 1 Model performance on predicting activation barriers of S_N2 in both full and minimal basis representations for def2-SVP and def2-TZVP basis sets

Basis set	Basis set type	Error
def2-SVP	Full	0.022 eV
def2-SVP	Minimal	0.021 eV
def2-TZVP	Full	0.023 eV
def2-TZVP	Minimal	0.021 eV
Baseline	—	0.152 eV

learning, implying that this linear interpolation strategy to determine transition state **C** from reactant and product **C**'s is a sufficient pre-processing step to the model.

While a constant value of p performs well for this dataset, it might be advantageous to incorporate further inductive bias into an approximated transition state structure. We propose an alternative interpolation scheme, which considers the reaction's ΔG to generate interpolated **R** and **C** at the transition state. The motivation for this interpolation scheme is Hammond's postulate[34] for organic reactions, which states that endergonic reactions have transition states that are product-like, while exergonic reactions have transition states that are reactant-like.

To encode Hammond's postulate into a model to generate p, we create a skewed normal distribution $\Phi(x) = 2f(x)g(x)$, where,

$$f(x) = \frac{1}{2}\left[1 + \operatorname{erf}\left(\alpha \frac{\frac{x-\mu}{\sigma}}{\sqrt{2}}\right)\right], \tag{6}$$

is a cumulative distribution function, where μ is the mean, σ is the standard deviation and α is a damping parameter, and

$$g(x) = \frac{1}{\sigma\sqrt{2\pi}}\exp\left(-\frac{1}{2}\left(\frac{x-\mu}{\sigma}\right)^2\right), \tag{7}$$

is a normal distribution. The skewed normal distribution is truncated at 0 (reactant-like) and 1 (product-like) to produce $h(x)$ as

$$h(x) = \frac{\Phi(x)}{f(1;\alpha=1) - f(0;\alpha=1)}. \tag{8}$$

Fig. 4c (lines) shows the behaviour of h for three different values of $\alpha(=\Delta G)$. At a very endergonic $\Delta G = 3$ eV (orange line), h is centred close to 1, indicating a high probability for the structure being product-like. Conversely, at a very exergonic $\Delta G = -3$ eV (blue line), h is centred close to 0, indicating a high probability of the structure being reactant-like; this behaviour is in line with Hammond's postulate. Finally, p is determined by taking a mean of a few randomly sampled points of $h(x)$ (coloured points in the distribution of Fig. 4c). Note that we sample this distribution to determine p, as opposed to, say, taking a moment of $h(x)$, to allow us to deal with varied reaction environments, which may be better described by several $h(x)$ functions instead of just one as we do here.

Fig. 4a and b (blue lines, $p \propto \Delta G$) shows the performance of this Hammond's postulate-inspired interpolation scheme in comparison to a constant value of p. Overall, the performance for **R** (Fig. 4a) is comparable to that of $p = 0.5$, with most structures having an MAE lower than 0.05 Å. Interpolations of **C** (Fig. 4b) yield similar performance as well. Since we are interested in predicting activation barriers and coefficient matrix elements (and not the transition state structure), we use fixed hyperparameter values of $\mu = 0.5$, $\sigma = 0.25$ and $\alpha = 1$ with ten randomly sampled points throughout this work. Further analysis of this method of determining an approximate transition
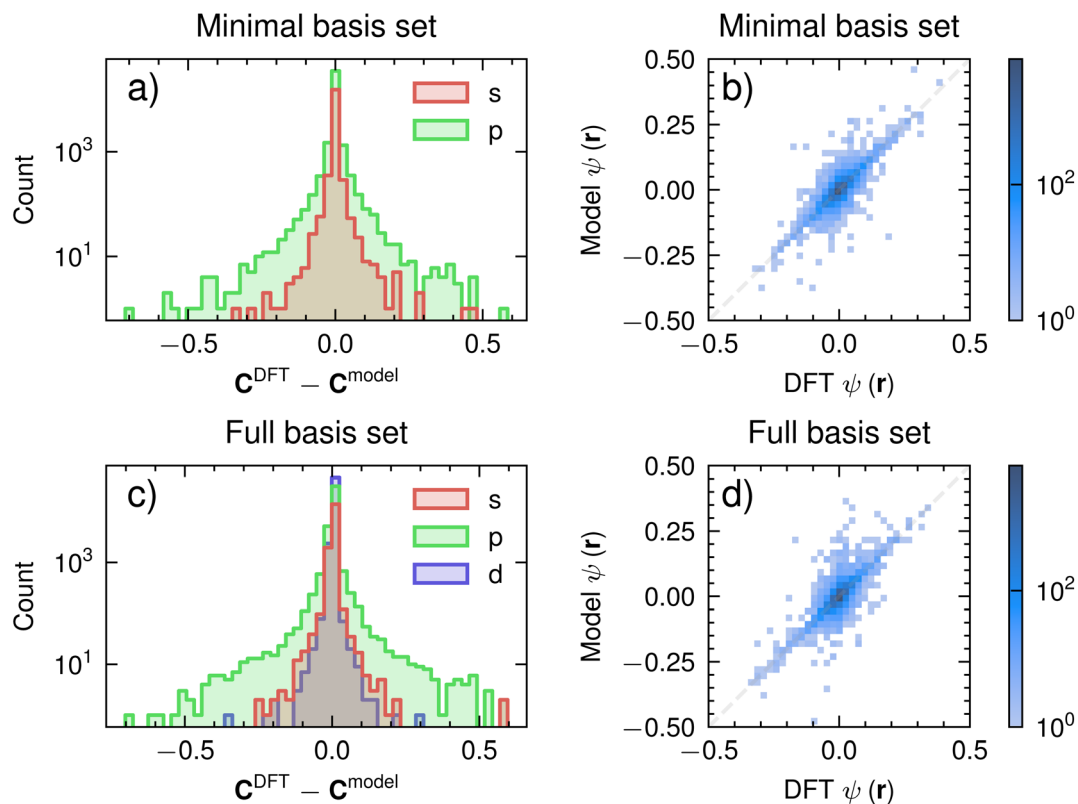
Fig. 7 Residual between the **C** from DFT and from the model for (a) minimal basis set (c) full basis set. Comparison of predicted and DFT values of the HOMO of the transition state sampled on a $4 \times 4 \times 4$ grid for a bounding box of 1.25 Å away from the farthest atom of each molecule in every direction for (b) minimal-basis representation (*i.e.* only s and p basis functions) (d) full-basis (*i.e.* as computed with DFT).

state is performed in Section S3† and illustrated in Fig. S9† for a more diverse dataset. However, the influence of the value of p may be reduced in such a comparison as significantly more input parameters (such as more coefficients) are used in the model.

C. *CoeffNet* architecture

We modify the equivariant network as implemented in ref. 33 to incorporate the constraints of **C** described in Section II. Fig. 5a shows a schematic of the constrained-network block that we use as a building block throughout *CoeffNet*. The inputs to the block are **C**, ν and **R** and the outputs are node features (**C**′) modified by weights, with the same dimensions of **C**. The first three operations (in red and blue) are consistent with ref. 33, where the edges are constructed based on a fixed cutoff, non-linearities are applied to the scalar quantities (gates), and convolutions are performed. The last block (in green) ensures that (1) entries in node features that come from padding to make the dimension of the node features equal are masked (*i.e.* set to zero and serve no role in the model), (2) this masked output is normalized such that its sum of squares is exactly one (both in line with the properties discussed in Section II).

To ensure that the network is equivariant with respect to rotations of the orbitals that make **C**, we generate appropriate irreducible representations to be fed into the network. The irreducible representation of the inputs is given by the

maximum number of s, p, d and higher functions that are present in each node feature. For example, if every node feature has one s, p and d function, the irreducible representation would consist of one $l = 0$ function with even parity, one $l = 1$ function with odd parity and one $l = 2$ function with even parity, in that order.

Fig. 5b shows a schematic of the architecture of *CoeffNet*. We start by supplying $\{\mathbf{C}, \nu, \mathbf{R}\}$ for reactants and products into two separate constrained network blocks. The outputs of these reactant and product blocks ($\mathbf{C}'_{\text{reactant}}$ and $\mathbf{C}'_{\text{product}}$ respectively) are averaged using $(1 - p)$ (reactant weight) and p (product weight) to generate an output for an interpolated transition state, $\mathbf{C}'_{\text{transition-state}}$. Interpolated transition state positions, $\mathbf{R}'_{\text{transition-state}}$ are generated through eqn (5). $\mathbf{C}'_{\text{transition-state}}$, ν and $\mathbf{R}'_{\text{transition-state}}$ are passed to another constrained network block to obtain the coefficients of the transition state, $\mathbf{C}_{\text{transition-state}}$. To obtain the activation barrier from this output, we elementwise subtract $\mathbf{C}_{\text{transition-state}}$ with $\mathbf{C}'_{\text{reactant}}$ and take the mean along the feature dimension. This subtraction is done to stay consistent with the definition of an activation barrier as the difference between the transition state and reactant energies.

D. Loss function

We use an MAE loss function for the task of predicting the activation energy and a custom *unsigned*-MAE loss function for
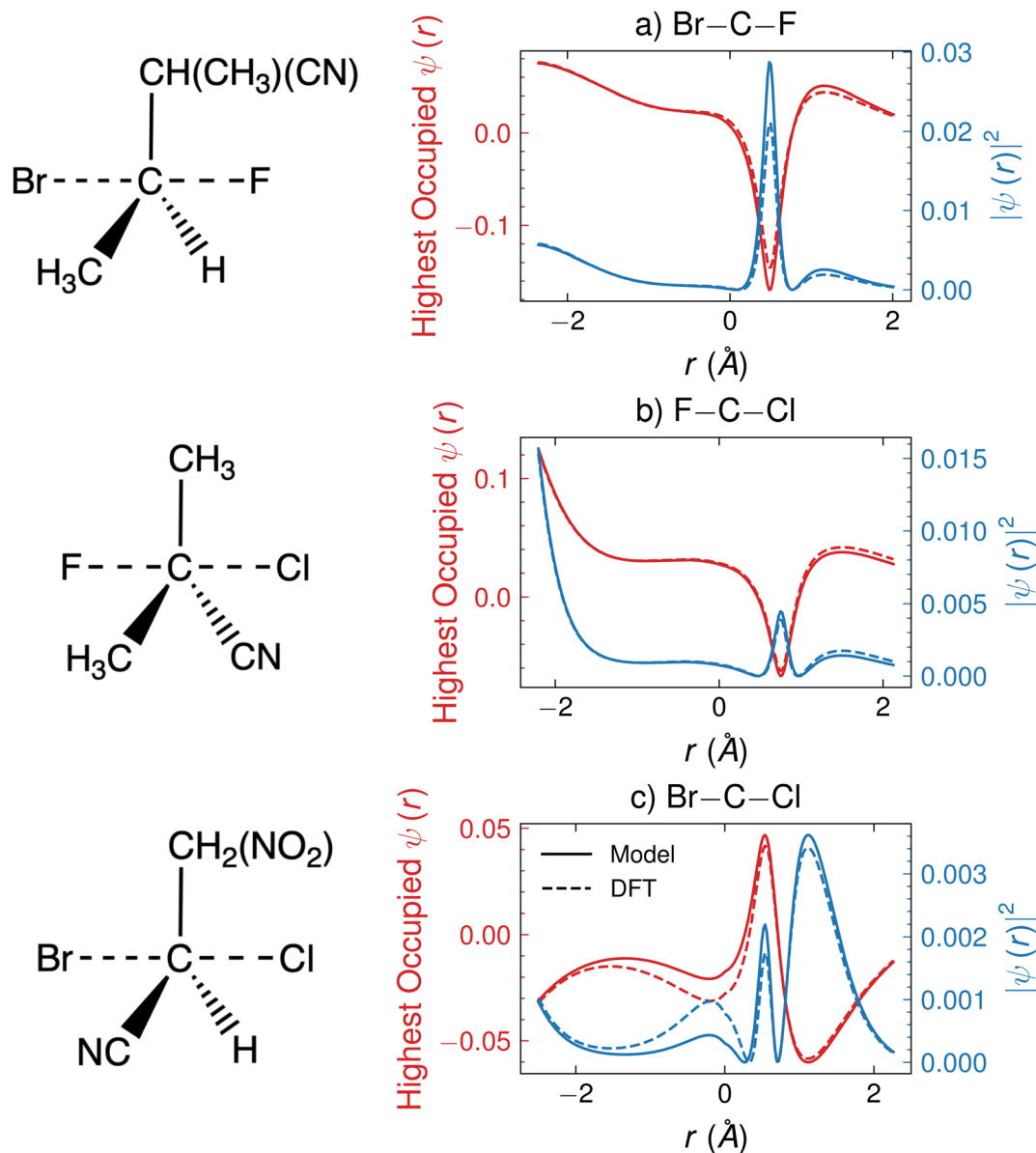
Fig. 8 Comparison of model-predicted and DFT (red) HOMO of the transition state and (blue) orbital density along the reaction axis of three S_N2 reactions between (a) attacking group F and leaving group Br (b) attacking group Cl and leaving group F (c) attacking group Cl and leaving group Br around a central carbon atom; images of the transition states are visualized to the left of the plots; left-most points on the x-axis indicate atom-centres of the leaving group and right-most positions indicate atom-centres of attacking groups at the transition state. Both model and DFT ψ are visualized in full-basis representation.

the task of predicting **C**. We define this *unsigned*-MAE loss function as,

$$\text{loss} = \sum_{i=1}^{N_{\text{basis}}} \min\{|\mathbf{C}^{\text{DFT}} - \mathbf{C}^{\text{Predicted}}|, |\mathbf{C}^{\text{DFT}} + \mathbf{C}^{\text{Predicted}}|\}. \quad (9)$$

where we continue to use the convention that **C** is a vector for a single molecular orbital for all atomic orbitals ($i \in [1, N_{\text{basis}}]$). The choice of this loss function (instead of an MAE) is due to the arbitrariness of the sign associated with the coefficient matrix (and, in general, with eigenvectors), as mentioned in Section II. Note that the choice of sign, either positive or negative, needs to be determined only once per graph, implying that the gradients

will not alternate through different signs with changing epochs. Fig. S8† shows that the training curves through this *unsigned*-MAE loss function is smooth and does not fluctuate, implying that this loss function is stable in its performance.

E. Model performance: activation barriers

We now report the performance of *CoeffNet* on the task of predicting the activation barrier on the S_N2 dataset computed with the def2-SVP basis set.[35] To demonstrate the working of *CoeffNet*, we choose this proof-of-concept dataset of S_N2 reactants taken from ref. 31 (see Section VI for further description and Section S4† for hyperparameter testing, Section S5† for

information about data-splits and Section S8† for corresponding plot for the def2-TZVP basis set). Our motivation for using this dataset as a basis for testing the performance of *CoeffNet* stems from the need for high-accuracy activation barrier prediction for a specific type of chemical reaction with limited number of elements.

Fig. 6a and b show the results of the activation barrier prediction task on both minimal basis and full basis representations, respectively, for the test set. Both models accurately predict the activation barrier computed with DFT calculations (*x*-axis) to within an accuracy of 0.025 eV (the mean activation barrier for the test dataset is 0.29 eV, see Fig. S4† for further information).

Table 1 shows the performance of the model with two different basis sets def2-SVP and def2-TZVP; the latter contains more basis functions than the former. To compare our results with a baseline, we fit a linear model between the activation barrier and the difference between the product and reactant energies (a form of BEP relations). Note that the baseline test does not learn the barriers very well (see Section S6† for further details); the relatively small numeric value of the error has to do with the range of activation energies considered in this dataset (most values are between 0 and 0.5 eV). Kernel-based machine learning models as in ref. 36 trained on a similar dataset has a mean absolute error of ∼0.25 eV. Recent implementations of message-passing neural networks using simpler and easier to obtain descriptors obtain an MAE of ∼0.11 eV.[37]

Both minimal and full basis models predict activation barriers for the S_N2 with low MAE. Applying a larger basis sets (def2-SVP → def2-TZVP) does not change errors in prediction significantly (0.022 *vs.* 0.023 eV). As expected, employing a larger basis set while operating on a minimal basis does not change the mean absolute error significantly (only changes beyond the third decimal place). Given that the performance of all models, irrespective of the basis set, is nearly identical (around 0.02 eV), it is preferable to use a minimal basis representation as it is much cheaper to train and requires fewer parameters during inference for the S_N2. Note that the prediction errors are distinct from those associated with differences in computed and experimental transition states. However, the errors from *CoeffNet* for this dataset are smaller than those between experiment and DFT calculations (∼0.08 eV for similar reactions with the B3LYP functional),[38] indicating that errors between our model and experiment are of similar orders of magnitude as between DFT calculations and experiments. We achieve this level of accuracy while training on the coefficients of a single eigenvalue (*i.e.* the HOMO) and hence do not need to add more parameters by using the coefficients of multiple eigenvalues as input. Furthermore, we note that *CoeffNet* has been tested only on a specific reaction class (*i.e.* the S_N2 reaction) and will most likely require further modifications before being applied to more diverse datasets. It is also likely that there might be reactions involving more complex species, such as organometallic compounds, which might require an input to *CoeffNet* consisting of a combination of multiple eigenstates to accurately predict their activation barriers.

Finally, we briefly discuss the performance of *CoeffNet* on a diverse dataset, consisting of several different reaction classes (as opposed to just a single reaction class, such as the S_N2 dataset discussed in this section). Note that the objective of training *CoeffNet* on a diverse dataset is to use its results as a pre-sieving strategy for high-throughput study of large reaction networks. For example, if *CoeffNet* predicts an activation barrier that is too large to be of chemical interest (typically >1 eV for reactions at room temperature) it is removed from further consideration in the reaction network. Conversely, if it predicts an activation barrier that indicates that the reaction is likely to occur, then the conventional computationally-intensive transition state search approaches are employed to determine the correct value of the activation barrier.

In order for *CoeffNet* to perform this pre-sieving role for high-throughput reaction networks, it must predict reasonably accurate transition state barriers with a small spread (*i.e.* a small standard deviation of the errors). We train *CoeffNet* on the dataset generated by ref. 25 and 39 (see Section S10† for a detailed discussion). We find that the MAE is 0.42 eV on a dataset which spans ≈10 eV, similar to the MAE of obtained with the $SLATM_d^{(2)}$ kernel and nearly double that of a trained directed message-passing neural network for slightly different dataset splits.[40] We do not perform extensive hyperparameter tests, instead we use the same parameters as listed in Section VI; while out of the scope of our current work, we expect that further hyperparameter and model tuning to be beneficial to reduce the mean absolute error for this dataset. Furthermore, we find that the standard deviation of the error to be 0.68 eV (corresponding to a root-mean-square error of 0.65 eV), well within the margin of error expected to accurately predict reactions of interest which can then undergo computationally intensive DFT and transition state finding calculations.

F. Model performance: predicting HOMO on a grid

Fig. 7 shows the model's performance in predicting the HOMO of the transition state. Fig. 7a and c show the signed error between the coefficients of the HOMO determined by DFT ($\mathbf{C}^{DFT}$) and those that are output from the model ($\mathbf{C}^{model}$) for the minimal and full basis set respectively. Most errors are between −0.2 and 0.2, indicating that the model learns the relative importance of each atomic orbital in the HOMO. There are a few select p-functions (less than 20 elements out of a possible approx. 6000 elements) that have considerable errors of less than −0.4 and more than 0.4 for both minimal and full basis representations. This large error in a small percentage of points likely stems from incorrectly learnt polarization functions (largely composed of p-orbitals). If highly accurate coefficients are needed, we suggest excluding polarization functions in the minimal basis representation or incorporating further constrained network blocks (*cf.* Fig. 5) to learn core and polarization functions separately. Given that our purposes are largely for interpretation (see Section IV), we suggest that this level of accuracy, from a relatively small dataset, is sufficient.

We now discuss the model's performance after using its output coefficients to generate the HOMO on a grid through eqn

(1). Fig. 7b and d shows a parity plot between the predicted and DFT ψ for the HOMO of the transition state for the minimal and full basis set, respectively. We generate a uniform grid of $4 \times 4 \times 4$ around the molecule to determine this ψ. Overall, we find that the test set predictions faithfully represent the DFT outputs on the grid for most of the points (darker colours in Fig. 7b and d represent a larger concentration of points). In the next section, we use this predicted HOMO to gain insight into S_N2 reactions and compare this insight with conventional chemical intuition.

IV. Model output coefficients of frontier orbitals are interpretable

In this section, we analyze the predicted HOMO for a few specific S_N2 reactions to illustrate the interpretive qualities of the outputs of *CoeffNet*. Fig. 8 shows ψ (in red) along a one-dimensional channel for three arbitrarily chosen reactions in the test dataset, F attacking and Br leaving in Fig. 8a (transition states are visualized to the left of the plot), Cl attacking and F leaving in Fig. 8b and Cl attacking and Br leaving in Fig. 8c; all occurring *via* a commonly bound carbon atom, which is bound to different species (such as H, CN, CH_3 and NO_2). The corresponding orbital densities, $|\psi|^2$, are shown in blue. The x-axis indicates the relative positions of the leaving group (left) to the attacking group (right) at the transition state structure, centred around the carbon atom (*i.e.* the carbon atom centre is at zero on the x-axis). In the reactant state, the attacking group has a charge of -1, and leaving group is bound to the carbon atom, while in the product state, leaving group has a charge of -1, and the attacking group is attached to the carbon atom. At the transition state, the attacking and leaving groups are at an intermediate distance from the carbon atom. Dashed lines indicate outputs from DFT, while solid lines indicate the outputs from *CoeffNet*. Consistent with the tests of Fig. 7b and d the model predicted and DFT ψ are very similar (*i.e.* the dashed and solid lines nearly overlap for all r).

We observe a peak in the orbital densities for the HOMO for all reactions shown in Fig. 8 between the central carbon atom at the attacking group (between 0 and 1 Å on the x-axis). This peak indicates the formation of a negatively charged substituent and is present irrespective of the character of the attacking group or the surrounding reaction environment around the carbon atom. Furthermore, certain reactions, such as in Fig. 8c, have peaks present near the attacking group atom ($\sim$1.5 Å on the x-axis), which is likely due to a large anionic character present on the chlorine atom at the transition state. Smaller secondary peaks are observed in Fig. 8a and b, indicating a weaker anionic character of these incoming substituents at this particular transition state. Anionic character is present in the leaving group as well; all reactions in Fig. 8 show an increase in the orbital density at the attacking group atom centre ($\sim$$-2$ Å), though their relative magnitude is given by their electronegativity (larger for fluorine in Fig. 8b and smaller for Br in Fig. 8a and c).[41] Note that the complexities of the task of predicting the activation barrier are represented by the lack of clear trends in orbital densities in Fig. 8, *i.e.* a combination of factors, such as electronegativity and

incoming and leaving groups and steric effects of ligands appear to influence chemical reactivity (and hence the barrier).

As *CoeffNet* facilitates predictions of activation barriers as well as ψ, we suggest that it can lead to interpretive arguments about patterns of chemical bonding present in a large dataset. We hypothesize that predictions of ψ can be used to determine if the model is incorrectly learning attributes of a certain reaction, thus offering checks and balances on the predicted activation barriers. Overall, we find that using $\mathbf{C}$ as a feature to *CoeffNet* allows us to interpret our model predictions in the context of known chemical bonding patterns, leading to more robust and interpretable predictions for a given class of reactions. Furthermore, we suggest that predictions of $\mathbf{C}$ could lead to easy initialization of a DFT calculation, allowing for a direct link to active-learning procedures to reduce the number of optimizer steps required to determine a transition state.

V. Conclusion

In this work, we introduce *CoeffNet*, an interpretable, equivariant and physically constrained graph neural network. *CoeffNet* uses the coefficients of a chosen molecular orbital of reactants and products to predict activation barriers as well as coefficients for the same molecular orbital of the transition state. We illustrate the different components of *CoeffNet*, starting with the interpolation routine to predict interpolated transition state quantities based on Hammond's postulate and the constraints to ensure that its node features can always be interpreted as coefficients. As a proof-of-concept, we test our model on an S_N2 dataset and show that the predicted activation barriers are accurate with respect to DFT calculations. Based on the S_N2 dataset, we show that the output molecular orbitals allow for chemically intuitive interpretations. Overall, we find that by using the coefficients of a molecular orbital as features, we gain accurate transition state predictions and an interpretive understanding of the chemical reactions in a dataset.

VI. Computational methods

Localized-basis density functional theory calculations were performed using the Q-Chem[42] (v5.4) software package. Workflows to perform these calculations were taken from the atom-ate[43] Python package and were facilitated through the fireworks[44] package. Parsing of all energies, Hamiltonian matrices, overlap matrices and coefficient matrices from Q-Chem output files were performed using pymatgen.[45]

The S_N2 dataset was taken directly from ref. 31. As these structures were computed with a different electronic structure code and transition states were determined using numerical frequencies, we recomputed the frequencies for all provided transition state structures. We re-optimized the transition states for all structures that did not have exactly one imaginary frequency using the FrequencyFlatteningTransitionStateFW implemented in atomate,[43] which computes the transition state structure and iteratively checks if exactly one imaginary frequency is present. We take all structures that contain one imaginary frequency (2178 total entries). We note that the

dataset in ref. 31 does not contain complexes in the product state. To determine these end states, transition state structures are perturbed along the eigenvectors scaled by −0.5 and 0.5. Constraints on atoms are used in line with ref. 31 to ensure that the halogen atoms do not abstract hydrogen atoms away from the carbon skeleton. After determining the structures, a single point with the different basis sets used in this study, *i.e.* def2-SVP and def2-TZVP,[35,46] were performed. Note that the def2 family of basis sets requires the use of effective core potentials (ECPs) for atoms heavier than Kr. No reactions using an ECP were included in the training set. While the inclusion of ECPs should change only the Kohn–Sham effective potential in the Hamiltonian, application of *CoeffNet* to reactions using heavier element ECPs may require further training. All calculations were performed with the B3LYP[47,48] functional in spin-restricted mode. The purecart = 1111 option was used to ensure that all calculations were performed in a spherical basis.

CoeffNet is written entirely in Python using the pytorch-geometric framework. Equivariant networks, consisting of convolution, activation (of scalars) and aggregation, were performed using the e3nn package. All training was performed on NVIDIA A100 GPUs. Further details on hyperparameter testing are shown in Section S4.† Tests were conducted on the S_N2 dataset using a random split of 80 : 10 : 10 train/validation/test set. Model parameters were optimized on the training set, hyperparameters are selected based on model performance on the validation set, and errors are reported using the test set unless otherwise stated. The Adam optimizer with a batch size of 8 with an initial learning rate of 0.001 was adopted. The learning rate is altered through the training process by a factor of 0.5 each time the learning rate plateaus for more than 10 epochs through the ReduceLROnPlateau function implemented in the torch python library.

Data availability

CoeffNet is freely available at **https://github.com/sudarshanv01/coeffnet**. Hamiltonian matrices, overlap matrices, coefficient matrices, eigenvalues and structures for all S_N2 reactions used in this work are available at **https://doi.org/10.5281/zenodo.10530180**.

Author contributions

Sudarshan Vijay: conceptualization, data curation, formal analysis, methodology, software, validation, visualization, writing – original draft, writing – review & editing. Maxwell Venetos: formal analysis, writing – review & editing. Evan Walter Clark Spotte-Smith: conceptualization, writing – review & editing. Aaron Kaplan: formal analysis, writing – review & editing. Mingjian Wen: formal analysis, writing – review & editing. Kristin Persson: conceptualization, funding acquisition, resources, writing – original draft, writing – review and editing.

Conflicts of interest

There are no conflicts to declare.

References

1 L. Xing and O. Borodin, Oxidation induced decomposition of ethylene carbonate from DFT calculations - importance of explicitly treating surrounding solvent, *Phys. Chem. Chem. Phys.*, 2012, **14**, 12838–12843.

2 E. W. C. Spotte-Smith, T. B. Petrocelli, H. D. Patel, S. M. Blau and K. A. Persson, Elementary decomposition mechanisms of lithium hexafluorophosphate in battery electrolytes and interphases, *ACS Energy Lett.*, 2023, **8**, 347–355.

3 E. W. C. Spotte-Smith, S. M. Blau, D. Barter, N. J. Leon, N. T. Hahn, N. S. Redkar, K. R. Zavadil, C. Liao and K. A. Persson, Chemical reaction networks explain gas evolution mechanisms in mg-ion batteries, *J. Am. Chem. Soc.*, 2023, **145**(22), 12181–12192.

4 J. L. Tebbe, T. F. Fuerst and C. B. Musgrave, Degradation of ethylene carbonate electrolytes of lithium ion batteries via ring opening activated by licoo2 cathode surfaces and electrolyte species, *ACS Appl. Mater. Interfaces*, 2016, **8**, 26664–26674.

5 M. D. Wodrich, M. Busch and C. Corminboeuf, Accessing and predicting the kinetic profiles of homogeneous catalysts from volcano plots, *Chem. Sci.*, 2016, 7, 5723–5735.

6 J. Lym, G. R. Wittreich and D. G. Vlachos, A Python Multiscale Thermochemistry Toolbox (pMuTT) for thermochemical and kinetic parameter estimation, *Comput. Phys. Commun.*, 2020, **247**, 106864.

7 E. Skúlason, G. S. Karlberg, J. Rossmeisl, T. Bligaard, J. Greeley, H. Jónsson and J. K. Nørskov, Density functional theory calculations for the hydrogen evolution reaction in an electrochemical double layer on the Pt(111) electrode, *Phys. Chem. Chem. Phys.*, 2007, **9**, 3241–3250.

8 E. D. Hermes, A. N. Janes and J. R. Schmidt, Micki: a python-based object-oriented microkinetic modeling code, *J. Chem. Phys.*, 2019, **151**, 014112.

9 J. Andersen and J. Mack, Mechanochemistry and organic synthesis: from mystical to practical, *Green Chem.*, 2018, **20**, 1435–1443.

10 T. Nakayoshi, K. Kato, S. Fukuyoshi, O. Takahashi, E. Kurimoto and A. Oda, Comparison of the activation energy barrier for succinimide formation from α-and β-aspartic acid residues obtained from density functional theory calculations, *Biochim. Biophys. Acta, Proteins Proteomics*, 2018, **1866**, 759–766.

11 X. Li, Z. Cai and M. D. Sevilla, Investigation of proton transfer within dna base pair anion and cation radicals by density functional theory (dft), *J. Phys. Chem. B*, 2001, **105**, 10115–10123.

12 H. B. Schlegel, Exploring potential energy surfaces for chemical reactions: an overview of some practical methods, *J. Comput. Chem.*, 2003, **24**, 1514–1527.

13 J. Bronsted, Acid and basic catalysis, *Chem. Rev.*, 1928, **5**, 231–338.

14 R. P. Bell, The theory of reactions involving proton transfers, *Proc. R. Soc. London, Ser. A*, 1936, **154**, 414–429.

15 M. G. Evans and M. Polanyi, Some applications of the transition state method to the calculation of reaction velocities, especially in solution, *Trans. Faraday Soc.*, 1935, **31**, 875–894.

16 P. N. Plessow and F. Abild-Pedersen, Examining the linearity of transition state scaling relations, *J. Phys. Chem. C*, 2015, **119**, 10448–10453.

17 A. O. Cohen and R. A. Marcus, Slope of free energy plots in chemical kinetics, *J. Phys. Chem.*, 1968, **72**, 4249–4256.

18 M. M. Melander, Grand Canonical Rate Theory for Electrochemical and Electrocatalytic Systems I: General Formulation and Proton-coupled Electron Transfer Reactions, *J. Electrochem. Soc.*, 2020, **167**, 116518, ISBN: 192.38.90.123.

19 S. M. Brown, M. J. Orella, Y. W. Hsiao, Y. Roman-Leshkov, Y. Surendranath, M. Z. Bazant, and F. Brushett, Electron Transfer Limitation in Carbon Dioxide Reduction Revealed by Data-Driven Tafel Analysis, *ChemRxiv*, 2020, preprint, DOI: **10.26434/chemrxiv.13244906.v1**.

20 S. Gosavi and R. A. Marcus, Nonadiabatic Electron Transfer at Metal Surfaces, *J. Phys. Chem. B*, 2000, **104**, 2067–2072.

21 S. Choi, Prediction of transition state structures of gas-phase chemical reactions via machine learning, *Nat. Commun.*, 2023, **14**, 1168.

22 T. Lewis-Atwell, P. A. Townsend and M. N. Grayson, Machine learning activation energies of chemical reactions, *Wiley Interdiscip. Rev.: Comput. Mol. Sci.*, 2021, **12**(4), e1593.

23 J. A. Garrido Torres, P. C. Jennings, M. H. Hansen, J. R. Boes and T. Bligaard, Low-Scaling Algorithm for Nudged Elastic Band Calculations Using a Surrogate Machine Learning Model, *Phys. Rev. Lett.*, 2019, **122**, 156001.

24 S. Heinen, G. F. von Rudorff and O. A. von Lilienfeld, Toward the design of chemical reactions: machine learning barriers of competing mechanisms in reactant space, *J. Chem. Phys.*, 2021, **155**, 064105.

25 C. A. Grambow, L. Pattanaik and W. H. Green, Deep Learning of Activation Energies, *J. Phys. Chem. Lett.*, 2020, **11**, 2992–2997.

26 K. A. Spiekermann, L. Pattanaik and W. H. Green, Fast Predictions of Reaction Barrier Heights: Toward Coupled-Cluster Accuracy, *J. Phys. Chem. A*, 2022, **126**, 3976–3986.

27 R. Jackson, W. Zhang and J. Pearson, Tsnet: predicting transition state structures with tensor field networks and transfer learning, *Chem. Sci.*, 2021, **12**, 10022–10040.

28 W. Yang, Direct calculation of electron density in density-functional theory, *Phys. Rev. Lett.*, 1991, **66**, 1438.

29 T. Stuyver and S. Shaik, Unifying conceptual density functional and valence bond theory: the hardness–softness conundrum associated with protonation reactions and uncovering complementary reactivity modes, *J. Am. Chem. Soc.*, 2020, **142**, 20002–20013.

30 E. P. Wigner, *Gruppentheorie und ihre anwendung auf die quantenmechanik der atomspektren*, 1931.

31 G. F. von Rudorff, S. N. Heinen, M. Bragato and O. A. von Lilienfeld, Thousands of reactants and transition states for competing e2 and s2 reactions, *Mach. Learn.: Sci. Technol.*, 2020, **1**, 045026.

32 L. A. Agapito, S. Ismail-Beigi, S. Curtarolo, M. Fornari and M. B. Nardelli, Accurate tight-binding hamiltonian matrices from ab initio calculations: minimal basis sets, *Phys. Rev. B*, 2016, **93**, 035104.

33 M. Geiger and T. Smidt, e3nn, Euclidean Neural Networks, *arXiv*, 2022, preprint, arXiv:2207.09453 [cs], DOI: **10.48550/arXiv.2207.09453**.

34 G. S. Hammond, A correlation of reaction rates, *J. Am. Chem. Soc.*, 1955, **77**, 334–338.

35 F. Weigend and R. Ahlrichs, Balanced basis sets of split valence, triple zeta valence and quadruple zeta valence quality for h to rn: design and assessment of accuracy, *Phys. Chem. Chem. Phys.*, 2005, **7**, 3297–3305.

36 S. Heinen, G. F. von Rudorff and O. A. von Lilienfeld, Transition state search and geometry relaxation throughout chemical compound space with quantum machine learning, *J. Chem. Phys.*, 2022, **155**(22), 221102.

37 E. Heid, K. P. Greenman, Y. Chung, S.-C. Li, D. E. Graff, F. H. Vermeire, H. Wu, W. H. Green, and C. J. McGill, *Chemprop: a machine learning package for chemical property prediction*, 2023.

38 A. D. Kaplan, C. Shahi, P. Bhetwal, R. K. Sah and J. P. Perdew, Understanding density-driven errors for reaction barrier heights, *J. Chem. Theory Comput.*, 2023, **19**, 532–543.

39 C. A. Grambow, L. Pattanaik and W. H. Green, Reactants, products, and transition states of elementary chemical reactions based on quantum chemistry, *Sci. Data*, 2020, **7**, 137.

40 K. A. Spiekermann, T. Stuyver, L. Pattanaik and W. H. Green, Comment on 'physics-based representations for machine learning properties of chemical reactions', *Mach. Learn.: Sci. Technol.*, 2023, **4**, 048001.

41 A. P. Bento and F. M. Bickelhaupt, Nucleophilicity and leaving-group ability in frontside and backside sn2 reactions, *J. Org. Chem.*, 2008, **73**, 7290–7299.

42 Y. Shao, Z. Gan, E. Epifanovsky, A. T. Gilbert, M. Wormit, J. Kussmann, A. W. Lange, A. Behn, J. Deng, X. Feng, D. Ghosh, M. Goldey, P. R. Horn, L. D. Jacobson,

I. Kaliman, R. Z. Khaliullin, T. Kuś, A. Landau, J. Liu, E. I. Proynov, Y. M. Rhee, R. M. Richard, M. A. Rohrdanz, R. P. Steele, E. J. Sundstrom, H. L. Woodcock, P. M. Zimmerman, D. Zuev, B. Albrecht, E. Alguire, B. Austin, G. J. O. Beran, Y. A. Bernard, E. Berquist, K. Brandhorst, K. B. Bravaya, S. T. Brown, D. Casanova, C.-M. Chang, Y. Chen, S. H. Chien, K. D. Closser, D. L. Crittenden, M. Diedenhofen, R. A. DiStasio, H. Do, A. D. Dutoi, R. G. Edgar, S. Fatehi, L. Fusti-Molnar, A. Ghysels, A. Golubeva-Zadorozhnaya, J. Gomes, M. W. Hanson-Heine, P. H. Harbach, A. W. Hauser, E. G. Hohenstein, Z. C. Holden, T.-C. Jagau, H. Ji, B. Kaduk, K. Khistyaev, J. Kim, J. Kim, R. A. King, P. Klunzinger, D. Kosenkov, T. Kowalczyk, C. M. Krauter, K. U. Lao, A. D. Laurent, K. V. Lawler, S. V. Levchenko, C. Y. Lin, F. Liu, E. Livshits, R. C. Lochan, A. Luenser, P. Manohar, S. F. Manzer, S.-P. Mao, N. Mardirossian, A. V. Marenich, S. A. Maurer, N. J. Mayhall, E. Neuscamman, C. M. Oana, R. Olivares-Amaya, D. P. O'Neill, J. A. Parkhill, T. M. Perrine, R. Peverati, A. Prociuk, D. R. Rehn, E. Rosta, N. J. Russ, S. M. Sharada, S. Sharma, D. W. Small, A. Sodt, T. Stein, D. Stück, Y.-C. Su, A. J. Thom, T. Tsuchimochi, V. Vanovschi, L. Vogt, O. Vydrov, T. Wang, M. A. Watson, J. Wenzel, A. White, C. F. Williams, J. Yang, S. Yeganeh, S. R. Yost, Z.-Q. You, I. Y. Zhang, X. Zhang, Y. Zhao, B. R. Brooks, G. K. Chan, D. M. Chipman, C. J. Cramer, W. A. Goddard, M. S. Gordon, W. J. Hehre, A. Klamt, H. F. Schaefer, M. W. Schmidt, C. D. Sherrill, D. G. Truhlar, A. Warshel, X. Xu, A. Aspuru-Guzik, R. Baer, A. T. Bell, N. A. Besley, J.-D. Chai, A. Dreuw, B. D. Dunietz, T. R. Furlani, S. R. Gwaltney, C.-P. Hsu, Y. Jung, J. Kong, D. S. Lambrecht, W. Liang, C. Ochsenfeld, V. A. Rassolov, L. V. Slipchenko, J. E. Subotnik, T. Van Voorhis, J. M. Herbert, A. I. Krylov, P. M. Gill and M. Head-Gordon, Advances in molecular quantum chemistry contained in the Q-Chem 4 program package, *Mol. Phys.*, 2015, **113**, 184–215, DOI: **10.1080/00268976.2014.952696**.

43 K. Mathew, J. H. Montoya, A. Faghaninia, S. Dwarakanath, M. Aykol, H. Tang, I.-h. Chu, T. Smidt, B. Bocklund, M. Horton, *et al.*, Atomate: a high-level interface to generate, execute, and analyze computational materials science workflows, *Comput. Mater. Sci.*, 2017, **139**, 140–152.

44 A. Jain, S. P. Ong, W. Chen, B. Medasani, X. Qu, M. Kocher, M. Brafman, G. Petretto, G.-M. Rignanese, G. Hautier, *et al.*, Fireworks: a dynamic workflow system designed for high-throughput applications, *Concurr. Comput. Pract. Exp.*, 2015, **27**, 5037–5059.

45 S. P. Ong, W. D. Richards, A. Jain, G. Hautier, M. Kocher, S. Cholia, D. Gunter, V. L. Chevrier, K. A. Persson and G. Ceder, Python Materials Genomics (pymatgen): a robust, open-source python library for materials analysis, *Comput. Mater. Sci.*, 2013, **68**, 314–319.

46 F. Weigend, F. Furche and R. Ahlrichs, Gaussian basis sets of quadruple zeta valence quality for atoms h–kr, *J. Chem. Phys.*, 2003, **119**, 12753–12762.

47 A. Becke, Density-functional thermochemistry. iii. The role of exact exchange, *J. Chem. Phys.*, 1993, **98**, 5648–5652.

48 P. J. Stephens, F. J. Devlin, C. F. Chabalowski and M. J. Frisch, Ab initio calculation of vibrational absorption and circular dichroism spectra using density functional force fields, *J. Phys. Chem.*, 1994, **98**, 11623–11627.